Heliyon 10 (2024) e26001

Contents lists available at ScienceDirect

Heliyon

journal homepage: www.cell.com/heliyon

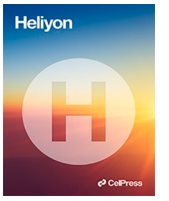

Research article

Performance domains of bio-inspired and triangular lattice patterns to optimize the structures' stiffness

Mathieu Bilhère-Dieuzeide [a,b], Julien Chaves-Jacob [a,*], Emmanuel Buhon [b], Guillaume Biguet-Mermet [b], Jean-Marc Linares [a]

[a] Aix-Marseille Univ, CNRS, ISM, Inst Mouvement Sci, UMR, 7287, Marseille, France
[b] Thales LAS (Land Air System) France OME (Optronics and Missile Electronics), Elancourt, France

ARTICLE INFO

Keywords:
Cellular structures
Bio-inspired design
Lattice structures
Material removal
Mechanical stiffness

ABSTRACT

Mass reduction of mechanical systems is a recurrent objective in engineering, which is often reached by removing material from its mechanical parts. However, this material removal leads to a decrease of mechanical performances for the parts, which must be minimized and controlled to avoid a potential system failure. To find a middle-ground between material removing and mechanical performances), material must be kept only in areas where it is necessary, for example using stress-driven material removal methods. These methods use the stress field to define the local material removal based on two local parameters: the local volume fraction v_f and the structural anisotropy orientation β. These methods may be based on different types of cellular structure patterns: lattice-based or bio-inspired. The long-term objective of this study is to improve the performance of stress-driven methods by using the most efficient pattern. For this purpose, this study investigates the influence of v_f and β on the mechanical stiffness of three planar cellular structures called Periodic Stress-Driven Material Removal (PSDMR) structures. The first, taken from the literature, is bio-inspired from bone and based on a square pattern. The second, developed in this study, is also bio-inspired from bone but based on a rectangular pattern. The third is a strut-based lattice pattern well documented in the literature for its isotropic behavior. These three patterns are compared in this study in terms of relative longitudinal stiffness, obtained through linear elastic compressive tests by finite element analysis. It is highlighted that each PSDMR pattern has a specific domain in which it performs better than the two others. In future works, these domains could be used in stress-driven material removal methods to select the most adequate pattern or a mix of them to improve the performances of parts.

1. Introduction

In mechanical engineering, mass reduction of parts is a current objective to save resources and improve the efficiency of systems. This objective can be reached by removing material from the part. However, the induced mechanical performances loss need to be understood and adapted to the loading case. Adequate mechanical performances once the material is removed from the part must be maintained.

In this context, several methods are presented in scientific works to obtain mass reduced parts. Among these methods, the most

* Corresponding author.
E-mail address: julien.chaves-jacob@univ-amu.fr (J. Chaves-Jacob).

https://doi.org/10.1016/j.heliyon.2024.e26001
Received 8 September 2023; Received in revised form 22 December 2023; Accepted 6 February 2024
Available online 13 February 2024

widely used is topology optimization [1]. This stress-driven method [2] allows reduce the mass based on slender beam structures [3,4]. Through mesh refining, and thus longer computing times, this method is able to remove material at a smaller scale [5]. At this scale, cellular porous structures, such as strut-based lattice or Triply Periodic Minimal Surfaces (TPMS) structures, are also used for material removal (MR). Strut-based lattice structures are based on struts jointed to one another to create the desired mathematical arrangements [6–10]. TPMS structures are based on mathematical rounded shapes design that are interconnected by nature [10–14]. Both methods tend to generate periodic structures. In terms of stiffness, TPMS present better overall mechanical performances than lattice [14,15]. They generate structures made of uniform struts or walls, which have a homogeneous thickness. Moreover, they can be used to design geometries that present different mechanical interests by varying the unit cell pattern, its size [16] or its thickness. For example, these methods propose the design of structures that have a great stiffness, that are great shock and energy absorber [17–20] or that are heat dissipater [21–23] or conductor [24]. In order to optimize the stiffness of structures, different methods can be combined. For example, topology optimization can be combined with lattices, TPMS or other cellular structures. One way to do so is that a unit cell is optimized through topology optimization and the part is substituted by repetition of this optimized unit cell [25–27]. Another way is that topology optimization defines the envelop of the final part and the remaining part is entirely substituted by a periodic repetition of the chosen unit cell [28–31].

To optimize the stiffness of structures, another suitable solution is to vary the local thickness of struts or walls of the unit cells of the periodic repetition (whether they are combined to the topology optimization or not) [23,32,33]. These alternative versions of the classic cellular structures are called “graded structures”. The gradient of strut or wall thickness can be stress-driven. Thus, the struts are thicker when the structure faces high intensity stresses (and inversely) [34,35].

In the category of stress-driven material removal methods, bio-inspiration may be used to provide new geometries. They can mimic structures having different sources.

- Vegetal sources: bamboo [36], pulvinus [37], pummelo pericarp [38], sea sponges [39], nautilus shell [40];
- Animal sources: toucan’s beak [41], fish bone structure [42], woodpecker’s beak [43], centriole coupled with nautilus shell [44], joints [45,46], bone [47–50].

For stiffness optimization, bones are often used as bio-inspiration due to their material frugality and their high mechanical

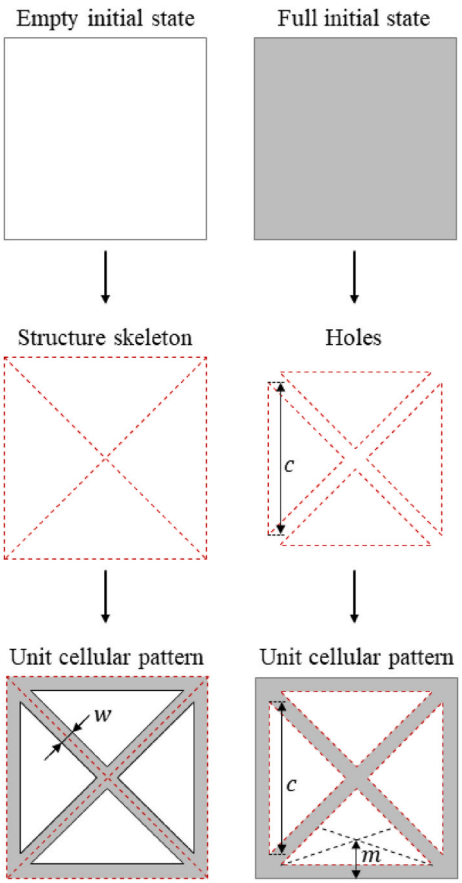

Fig. 1. Two ways of design to obtain the same unit cellular pattern.

performances. Bones tend to use a minimal amount of resources to generate maximal performances. In addition, their remodeling process is also a point of interest for mechanical designs. Numerous research works investigate bone structure to design bio-inspired structures. Particularly, long bones are largely studied. This type of bones undergoes similar mechanical loading, and thus similar mechanical stresses, as mechanical parts [51,52]. Studies highlighted that the morphogenesis process generates a global bone shape that is able to support the undergone stresses. This process is also involved to generate specialized areas such as the diaphysis region with its dense cortical bone surrounding the medullar cavity, and the epiphysis region with its trabecular porous bone [53]. Thus, long bones can be considered as stress-driven structure. Consequently, the bio-inspired method derived from the long bones morphogenesis process is qualified as stress-driven material removal method.

In the literature presented right above, plenty of studies focus on the comparison of mechanical performances of cellular structure such as uniform and graded lattice (strut or TPMS based). In addition, several works exist on the performance comparison of structures designed using bio-inspiration or topology optimization. However, structures bio-inspired from long bones (based on elliptical porosities) have not been compared to lattice structures.

This study investigates the mechanical performances of patterns generated using planar stress-driven cellular structures under uniaxial compression loads. It proposes a comparison of the mechanical properties of three geometrical structures derived from Periodic Stress-Driven Material Removal (PSDMR) patterns. A first pattern (from Ref. [47]) is bio-inspired from long bone structure and based on a square pattern. A second bio-inspired pattern based on a rectangular pattern (created to be an improvement of the first pattern) is developed in this study. A third pattern is a strut-based lattice type structure selected for its isotropic behavior. TPMS are not taken into account in this planar study due to their 3D topology. The objective of the study is to establish the performance domains of the three planar PSDMR patterns to determine which one has the best mechanical stiffness performances depending on its volume fraction and structural anisotropy orientation. In a first section, the periodic cellular geometries and the design parameters are presented (section 2). In a second section, the tested patterns are presented (section 3). In a third section, the FEA environment and associated parameters are defined, and simulation results are experimentally validated (section 4). The last sub-section focuses on the evaluation of the mechanical performances of PSDMR patterns (section 4.4). A last section discusses the most suitable domain of use for each PSDMR pattern depending on volume fraction and structural anisotropy orientation (section 5).

2. Periodic Stress-Driven Material Removal (PSDMR) method

2.1. Unit cellular pattern definition

A periodic cellular geometry can be described as a repetition of a unit cellular pattern. This unit cellular pattern is made of areas filled with material that adjoin areas made of void (Fig. 1). The initial state of the unit cell may be defined in two different ways.

- Empty initial state: in an elementary space made of void, the skeleton of the desired structure is defined. It is then thickened by a defined width *w* to obtained the final desired structure;
- Full initial state: in an elementary space filled with material, holes are created. Their shape, size and position define the final desired structure.

These two ways of design are equivalent and they lead to the same final geometry. For ease of unit cellular pattern numerical implementation, the full initial state is considered in this paper.

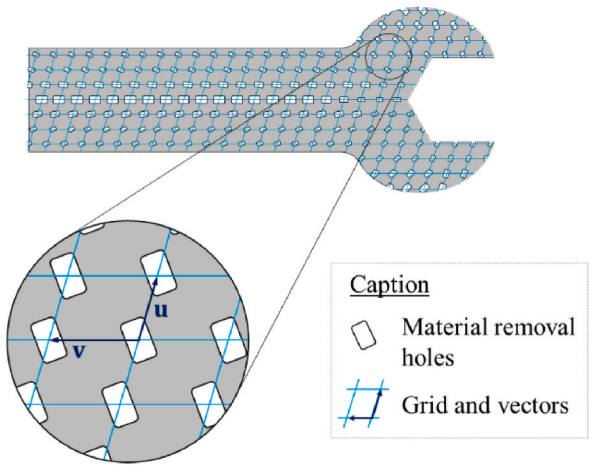

Fig. 2. General periodic mass removal method using a parallelepipedic grid and rounded rectangular MR holes as global periodic MR patterns, applied on an open-end wrench.

2.2. Periodic material removal pattern definition

Using the full initial state process, the periodic material removal (MR) pattern is defined by two geometrical elements (Fig. 2).

- The grid, used to define the positions of the future MR holes in the part. It is defined by two vectors **u** and **v**. The angle between these two vectors is a parameter defined by the user, as well as their norm. The angle between **u** and **v** allows to define the shape of the grid, and their norm to define the size of the grid. It is also oriented in the general coordinate system. In a periodic MR method, these parameters are fixed and constant. Therefore, the grid is uniform: it has a constant shape, size and orientation all over the part. Each unit element of the grid is called "grid mesh";
- The MR holes, that refers to the shape according to which the material is removed from the grid meshes. The positions of these holes are defined by the topology of the grid: in general, the holes are located on the nodes of the grid.

In the example shown in Fig. 2, a periodic MR pattern use case is represented. It is made of a parallelepipedic grid and rounded rectangular MR holes that are located on each node of the grid.

2.3. Local volume fraction and structural anisotropy orientation definitions

A Periodic Stress-Driven Mass Removal (PSDMR) method, which is based on the repetition of periodic MR pattern, computes local functional parameters depending on the mechanical stress field of the filled part. These parameters, which are computed in each grid mesh of the PSDMR pattern, are used for local adaptation of the pattern. There is two levels of local adaptation.

- First level: the local material density may vary and the part presents a controlled local volume fraction (section 2.3.1);
- Second level: the local structural orientation may vary and the part presents a controlled anisotropy orientation (section 2.3.2).

In stress-driven method, the process used to determine PSDMR pattern parameters can be split in six steps.

- Definition of the boundary conditions applied to the part;
- Estimation of the mechanical stress field;
- Definition of the grid (section 3.1);
- Calculation of the local volume fraction in each grid mesh, depending on the local mechanical stress;
- Determination of the local structural anisotropy orientation based on the mechanical stress field (section 2.3.2);
- Calculation of the design parameters of the MR holes based on the volume fraction, the structural anisotropy orientation and the grid design (section 3.2).

In a PSDMR method, at each point of the part, a couple of parameters $(v_f; \beta)$ is computed from the local stress field study. This couple of parameters will be presented subsequently.

2.3.1. Volume fraction v_f

The first level of local adaptation to the stress in PSDMR method is the variation of the material volume fraction v_f in each grid mesh. In this planar study, the volume fraction v_f is represented as the ratio of the remaining material surface in a single grid mesh over the total surface of this mesh (Eq. (1) and Eq. (2)).

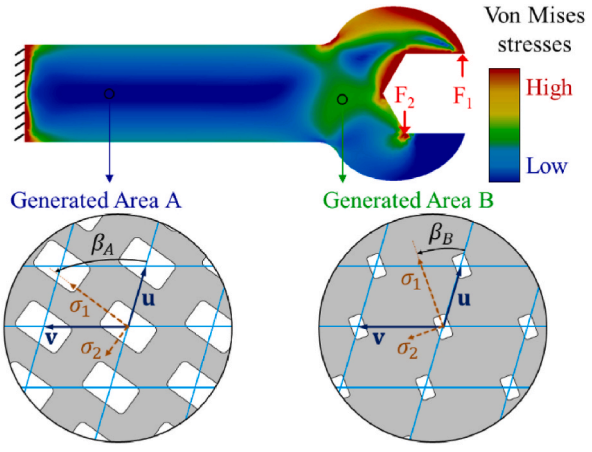

Fig. 3. Von Mises stress field on an open-end wrench submitted to forces simulating torque. Focus on two PSDMR areas: Area A with large material removal holes oriented of an angle β_A and Area B with smaller material removal holes oriented of an angle β_B:

$$v_f = \frac{S_{remaining\ material}}{S_{grid\_mesh}} \tag{1}$$

$$S_{remaining\_material} = S_{grid\_mesh} - S_{MR\_holes} \tag{2}$$

The PSDMR method adapts the volume fraction v_f to the local mechanical stress. In Fig. 3, area A presents a low intensity local stress, thus the resulting MR holes are large while area B presents a higher intensity local stress, thus the resulting MR holes are smaller.

2. 3.2. Structural anisotropy and structural anisotropy orientation β

At a second level, to improve the local adaptation to the mechanical stresses, anisotropy may be introduced and its orientation may be controlled [47,49,54,55].

2.3.2.1. Structural anisotropy in PSDMR method. To obtain this anisotropy, two ways are possible.

- Material anisotropy: it is obtained by the material itself (as in composite materials for example). This approach is difficult to implement in stress-driven method because the orientation of the material anisotropy needs to vary at each point of the part;
- Structural anisotropy: it is obtained by the non-uniform repartition of the remaining material in several directions. This property can be obtained by realizing non-uniform holes, in position or geometry (elliptic holes for example). It induces structural anisotropy which orientation is defined by an angle to the grid vectors called in the following "structural anisotropy orientation". In other terms, "structural anisotropy" defines the anisotropy of the pattern induced by the holes and not the anisotropy of the micro-structure of the used material. In this paper, only structural anisotropy is used.

On a same structure, a variation of structural anisotropy orientation may lead to different mechanical properties of the structure along a direction. Along a studied direction, the structure may be stiff with one orientation and bendable with another. Thus, for a given mechanical stress field, a direction along which the local stiffness is maximal exists: the stiffer direction. In addition, the structural anisotropy can be global (the same all around the structure) or local (locally different and independent in each grid mesh). In PSDMR method, the structural anisotropy is local and the structure orientation in each grid mesh depends on the local mechanical stress field.

2.3.2.2. Structural anisotropy orientation β. At each point of a structure, the mechanical stress field may be described by a tensor. In planar studies, this tensor is defined by two principal stresses of the principal coordinate system and by their associated direction. Usually, these two principal stresses are noted σ_1 and σ_2 such as $|\sigma_1| > |\sigma_2|$. To quantify this stress orientation to the grid, hereafter, the angle between $\boldsymbol{\sigma_1}$ and the **u**-axis of the mesh of the grid is set as β (Fig. 3). Moreover, this study is driven by the search for stiffness increase. In order to design structure for which the stiffness is maximized, the stiffer direction induced by structural anisotropy is aligned to the stress orientation. For example, in the case of Fig. 3, the stiffer direction is defined by the orientation of the longer side of the MR holes. Thus, hereafter, structural anisotropy orientation is characterized by the angle β. The PSDMR method adapts the structural anisotropy to the local major principal stress orientation. Indeed, in both areas, the MR holes are aligned to the σ_1 direction. It entails that the two areas have a different local structural anisotropy orientation β (Fig. 3).

3. PSDMR pattern specifications

To compare the different PSDMR patterns, these patterns must be presented and detailed.
In this study, uniaxial compression loading case is chosen. The mechanical stress field induced by this loading case is homogeneous

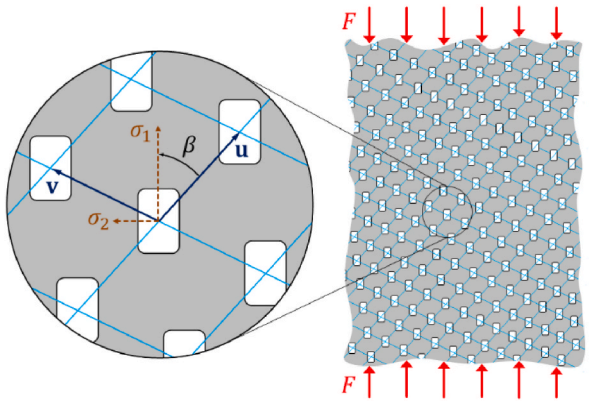

Fig. 4. Uniaxial compression on a local area of a mass reduced mechanical part.

in intensity (far from the application points). In addition, the major principal stress σ_1 is aligned along the loading direction (vertical hereafter). Consequently, the MR holes of the patterns have the same size and the same orientation. Thus, to vary the structural anisotropy orientation β, the grid of the patterns must be rotated by this angle β generating a grid orientation (Fig. 4).

3.1. Designed grids

The three PSDMR patterns defined in the study use grids of parameters L and l the sides of the quadrilateral such as $L = \|\mathbf{u}\|$ and $l = \|\mathbf{v}\|$. They can be designed in two different ways:

- Parallelepiped grids made of two adjacent triangles (isosceles or equilaterals) with MR holes at each node of the grid (purple grids in Fig. 5);
- Orthogonal grids with a topology that mimics a “face-centered" structure. The MR holes are located at each node of the grid as well as in the center of the grid mesh (blue grids in Fig. 5).

Hereafter, for understanding purposes, the grids are defined as orthogonal grids (in accordance with the second way of design). Using these orthogonal grids, two grid types can be defined.

The first grid defined in this study is a square-shaped grid [47,49,52] (Fig. 5a) that has the following properties.

- Its directional vectors $\mathbf{u}$ and $\mathbf{v}$ have the same norm; so in this grid, $L = l$;
- It has an angular periodicity of 90°. In fact, the grid varies in the range $[0°;\ 45°]$ and then symmetrical grids are obtained in the range $[45°;\ 90°]$. For this reason, in the following, this grid is only studied for angles varying in the range $[0°;\ 45°]$.

The second grid is a rectangular-shaped grid (Fig. 5b) specifically designed to obtain a regular hexagonal shape. It has the following properties.

- Its directional vectors $\mathbf{u}$ and $\mathbf{v}$ have different norms such as $L = l * \sqrt{3}$;
- Its topology and dimensions mean that the centers of the neighboring MR holes are equidistant unlike square-shaped grid. This rectangular grid can be redefined as a hexagonal grid made of six equilateral triangles; it has an angular periodicity of 60°. In fact, the grid varies in the range $[0°;\ 30°]$ and then symmetrical grids are obtained in the range $[30°;\ 60°]$. For this reason, in the following, this grid is only studied for angles varying in the range $[0°;\ 30°]$.

3.2. Designed material removal holes

The three PSDMR pattern defined in the study use two types of MR holes.

The first type of MR hole is elliptical-shaped (Fig. 6a). These holes are bio-inspired from long bone trabecular holes as presented in the literature [47]. It is defined by the length of its two semi-axis: a the major and b the minor [49,52]. This MR hole has the following properties:

- It exists in the same way in the two grids developed in section 3.1;
- It is oriented along the direction of the stress field in the initial filled structure induced by the uniaxial compression, so vertically;
- To increase the stiffness of the PSDMR pattern in uniaxial compression, the major semi-axis a, is aligned along the compression direction;
- Considering the compression loading case, $|\sigma_1| \gg |\sigma_2|$, an important structural anisotropy is needed in the compressive direction to insure a great stiffness. This structural anisotropy orientation can be obtained using very slender MR holes. For that, using the limit

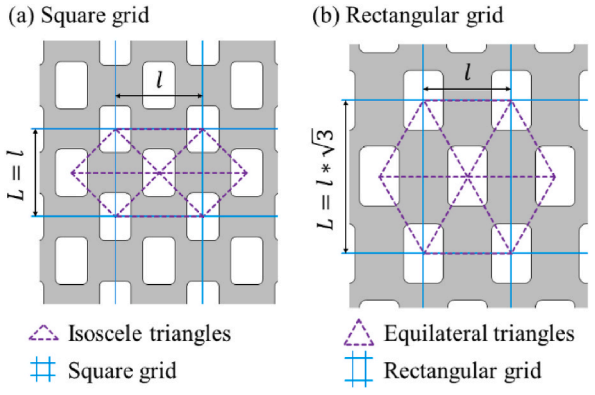

Fig. 5. Grids used in this study: the square-shaped grid (a) and the rectangular-shaped grid (b).

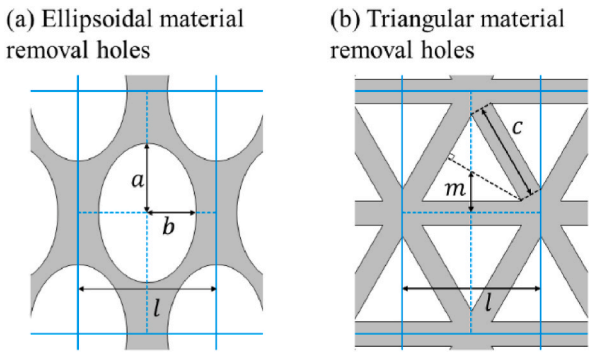

Fig. 6. Material removal holes used in this study: the elliptical-shaped holes (a) and the triangular-shaped holes (b).

of the bio-inspired relationship proposed in Ref. [47], the ratio a/b of the elliptic MR holes is set equal to 1.6. This ratio is called the form factor *FF* (Eq. (3));

- In the designed pattern, the volume fraction is set. Knowing the dimensions of the grid, the form factor *FF* and the volume fraction v_f, the two semi-axis length are derived from Eq. (3) and Eq. (4).

$$FF = \frac{a}{b} \tag{3}$$

$$a = \sqrt{\frac{L * l * FF * (1 - v_f)}{2 * \pi}} \tag{4}$$

The second type of MR hole is composed of two identical back-to-back equilateral triangles (Fig. 6b). It has the following properties.

- Its shape is devised and is aligned along the **u**-axis of the grid to provide a consistent structure;
- c is the length of the side of the triangles;
- m is the distance between the middle of the grid mesh and the barycenter of the triangles;
- To generate a strut-based lattice structure with regular strut thickness, the rectangular grid (section 3.1) must be used and the parameter m must verify Eq. (5);
- In the designed pattern, the volume fraction is set. Knowing the dimensions of the grid and the parameter m, the length of the side of the triangles c is derived from Eq. (6).

$$m = \frac{L}{6} \tag{5}$$

$$c = l * \sqrt{1 - v_f} \tag{6}$$

3.3. Computed PSDMR patterns

Combining the two possible type of grid (section 3.1) and the two type of material removal (MR) holes (section 3.2), three homogeneous PSDMR patterns are defined in this study.

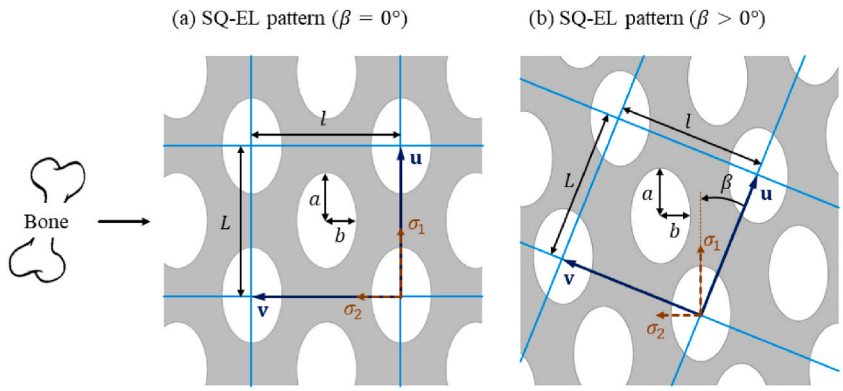

Fig. 7. Bone bio-inspired SQ-EL pattern using a structural anisotropy orientation $\beta = 0°$ (a) and $\beta > 0°$ (b).

- SQ-EL composed of a square grid and elliptical MR holes (Fig. 7a);
- RE-EL composed of a rectangular grid and elliptical MR holes (Fig. 8a);
- RE-TR consisting of a rectangular grid and triangular MR holes (Fig. 9a) and inspired by bi-pyramidal lattice structures (VBCC structure in Ref. [56]).

To ensure the comparison of all three PSDMR patterns, the length of the small side of the grid l is set equal for the three patterns.

In Figs. 7, Figs. 8 and 9, the compression direction is vertical. On the one hand, as specified in section 3.2, in the SQ-EL and RE-EL patterns, the major semi-axis of the ellipses are also vertical for any structural anisotropy orientation β (Figs. 7b and 8b). On the other hand, in the RE-TR pattern, as defined in section 3.2, the triangular MR hole is not oriented along the vertical direction (Fig. 9b).

4. Experiments to determine the performance domains of PSDMR patterns

4.1. Parameters variation

In this study, the mechanical performances of planar PSDMR patterns are compared and their performance domains are established. This comparison of performances has three variables.

- The three used PSDMR patterns: SQ-EL, RE-EL or RE-TR (section 3.3);
- The volume fraction v_f (section 2.3.1), that varies from 0.05 to 0.95 by 0.05 steps;
- The structural anisotropy orientation β (section 2.3.2) which depends on the grid shape (section 3.1): the two grids have distinct value of periodicity. In this study, five values are considered, regularly spread, in the periodicity range. Consequently, the square grid is studied in the range $[0°;\ 45°]$ by $11.25°$ steps and the rectangular grid is studied in the range $[0°;\ 30°]$ by $7.5°$ steps.

4.2. Structural cohesion limitations

Taking into account the range of variation of the two parameters v_f and β (section 4.1), structural cohesion issues may appear in the patterns involving the use of the elliptic holes. Indeed, due to the regular position of the elliptic holes, if holes intersect in a unit cellular pattern, then it causes an infinite split of the PSDMR pattern. If this phenomenon occurs, the cohesion of the structure is lost and the resulting structure has no mechanical resistance [47,49].

As shown in Fig. 10, in the case of the couple $(v_{f_2};\ \beta_1)$, marked with green backgrounds, structural cohesion in the pattern is ensured. On the one hand, from this cohesion case, a decrease of volume fraction v_f (from v_{f_1} to v_{f_2} in Fig. 10) that is too important induces a loss of structural cohesion. On the other hand, from a cohesion case, a variation of the structural anisotropy orientation β may also lead to a loss of structural cohesion (from β_1 to β_2 in Fig. 10). In addition, these situations are favored by low volume fractions.

Structural cohesion loss is illustrated for the three PSDMR patterns for tested couples $(v_f;\ \beta)$ in Fig. 11. The red backgrounds refer to the patterns that lost cohesion and the green backgrounds to the ones that did not. In case of non-cohesion, under loading conditions, the pattern collapses without any resistance. As expected, the RE-TR pattern is not subjected to this structural cohesion loss issue. Indeed, as explained in section 3, this pattern is a lattice structure by nature, so the MR holes do not intersect.

Finally, for each pattern involving elliptic MR holes (SQ-EL and RE-EL), there are couples $(v_f;\ \beta)$ for which the structural cohesion is lost. Table 1 highlights the couples for which the structural cohesion is lost with red boxes, and the couples for which the structural

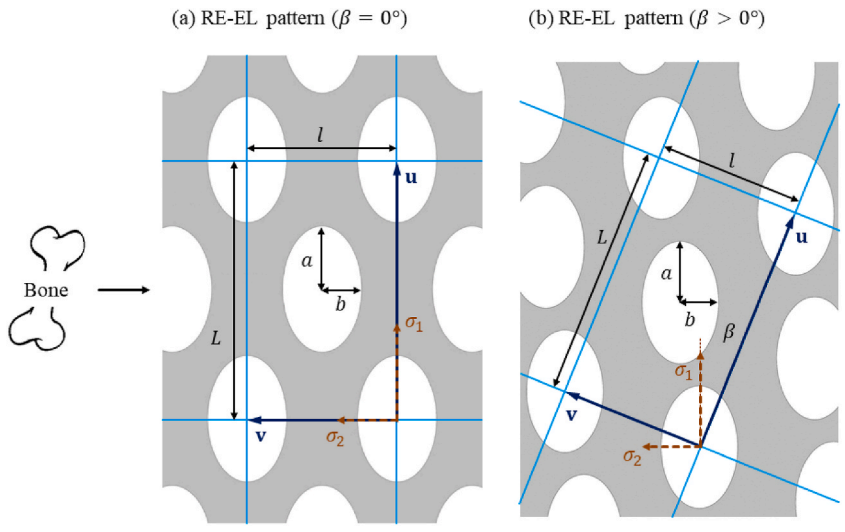

Fig. 8. Bone bio-inspired RE-EL pattern using a structural anisotropy orientation $\beta = 0°$ (a) and $\beta > 0°$ (b).

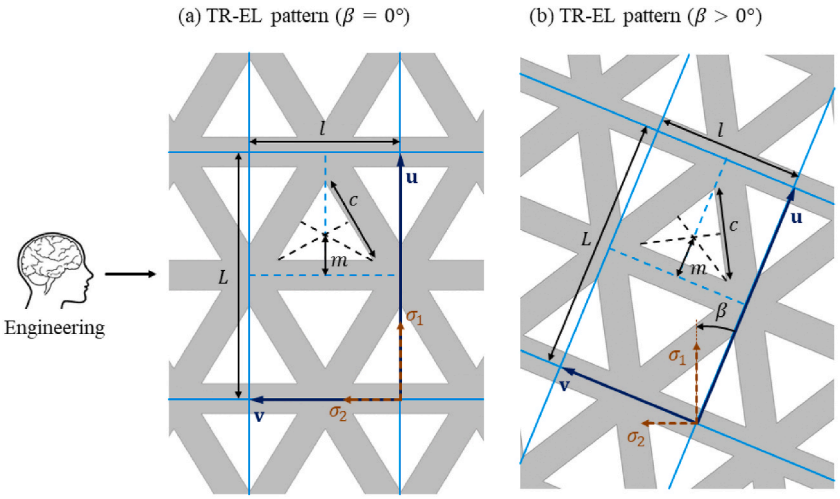

Fig. 9. Lattice RE-TR pattern using a structural anisotropy orientation β = 0° (a) and β > 0° (b).

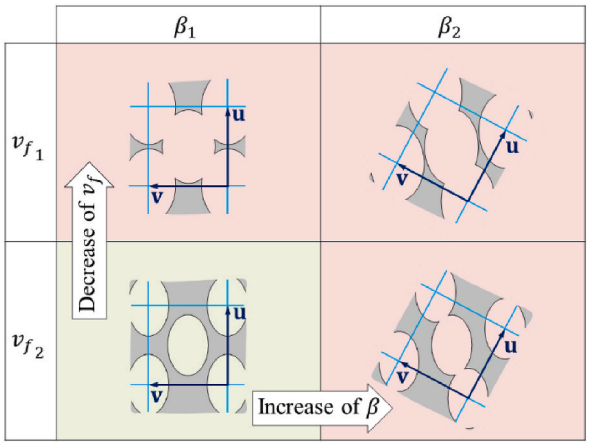

Fig. 10. Ways of reaching structural cohesion loss on a PSDMR pattern: decrease of the volume fraction v_f (from bottom to top) and/or increase of the structural anisotropy orientation β (from left to right).

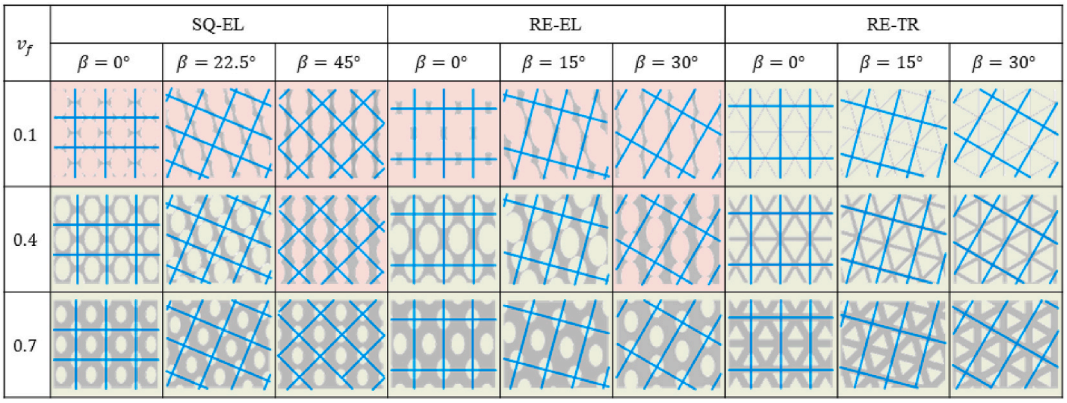

Fig. 11. PSDMR patterns for different combinations of the couple of parameters (v_f; β). The green backgrounds represent the pattern associated to a couple that ensures structural cohesion in the pattern. Inversely, the red backgrounds represent the pattern associated to a couple for which the structural cohesion is lost

Table 1
Summary of the structural cohesion of different PSDMR pattern depending on the couple (v_f; β). Green backgrounds highlight pattern presenting structural cohesion and red backgrounds highlight pattern presenting structural cohesion loss.

v_f	SQ-EL					RE-EL					RE-TR				
	Square grid + Elliptic holes					Rectangular grid + Elliptic holes					Rectangular grid + Triangular holes				
	$\beta_{SQ\text{-}EL}$					$\beta_{RE\text{-}EL}$					$\beta_{RE\text{-}TR}$				
	0°	11.25°	22.5°	33.75°	45°	0°	7.5°	15°	22.5°	30°	0°	7.5°	15°	22.5°	30°
0.05															
0.10															
0.15															
0.20															
0.25															
0.30															
0.35															
0.40															
0.45															
0.50															
0.55															
0.60															
0.65															
0.70															
0.75															
0.80															
0.85															
0.90															
0.95															

cohesion is ensured with green boxes. Only the couples that ensure structural cohesion are considered in the following of the study.

4.3. Finite Element Analysis environment calibration

This section studies the potential of Finite Element Analysis (FEA) environment for PSDMR pattern comparison (section 4.4). First, a specific set of nine samples (non-standardized) is developed and experimentally tested. Second, the FEA environment is presented and the nine samples are numerically tested under compressive loading. Finally, the potential of the FEA environment is validated.

4.3.1. Sample design and experimental tests

The samples consist in a central area from which material is removed using the three PSDMR patterns defined in section 3.3 and two bases. These bases are added at each side of the central part for experimental purposes. They ensure the interface between the central area and the rigid pressure plates during the compressive loads. The resulting samples have overall dimensions of 70 mm of height, 50 mm of width and 20 mm of thickness (Fig. 12).

The patterns used in the central area of the samples are set for a wide range of couples (v_f; β). These couples are set to ensure the structural cohesion (green boxes in Table 1). Nine samples are tested hereafter: three couples for each PSDMR pattern, at extreme structural anisotropy orientation and at low volume fractions (Fig. 16). The metric used to compare the samples is the relative stiffness (r_{exp} for the experiment tests and r_{FEA} for the numerical simulations).

For experimental tests, the nine designed samples are additively manufactured through MEX-TRB/P/PLA (polylactic acid material extrusion with thermal reaction bonding) as defined in the ISO/ASTM-52900:2021 standard (Fig. 12). All the nine samples are manufactured under the same conditions and parameters.

- Printer: Volumic STREAM 30 Dual Mk.2;

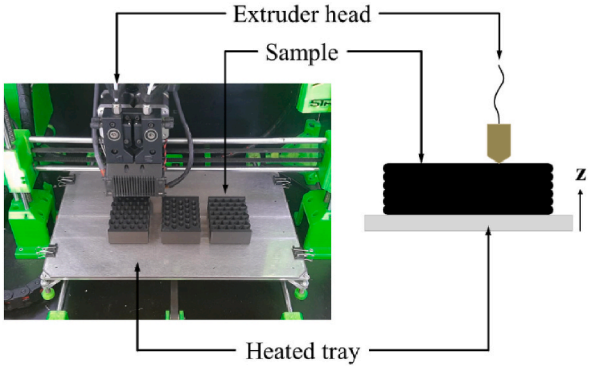

Fig. 12. Printing set-up used in the study.

- Material: polylactic acid (PLA) compound ("UNIVERSAL ULTRA – PLC") (density of the printed material equal to $1,308.35$ kg/m^3);
- Printing direction: $+\vec{z}$;
- Layer thickness: 0.15 mm;
- Infill percentage: 100%.

These printing conditions and parameters insured accurate printings of the sample regarding to their mass (Table 2).

Experimental tests of these samples consist in compression tests in linear elastic conditions (Fig. 13). The test bench is composed of a multicomponent dynamometer on which the sample is placed under uniaxial vertical compression. A displacement d_{exp} is imposed to the sample through rigid pressure plates. The sample compresses against the dynamometer that records the resulting force F_{exp}. Using these two quantities, the stiffness k^*_{exp} (in N/mm) of the sample is computed (Eq. (7)). Thereafter, this stiffness is divided by the stiffness k_{exp} of an additively manufactured filled sample without MR holes ($k_{exp} = 15,182$ N/mm). The division of the stiffness k^*_{exp} by the stiffness k_{exp} leads to the relative stiffness of the sample r_{exp} (Eq. (8)). Finally, for each of the nine samples studied through experimental tests, the ratio r_{exp} can be computed.

$$k^*_{exp} = \frac{F_{exp}}{d_{exp}} \tag{7}$$

$$r_{exp} = \frac{k^*_{exp}}{k_{exp}} \tag{8}$$

4.3.2. Finite element analysis environment and simulations

The FEA environment used to conduct the simulations is Siemens NX 11.0.2.7 that uses a Nastran solver. These structural simulations are done in linear elasticity conditions, ensuring that the material undergoes only elastic deformation and no plastic deformation. The Young's modulus used in the FEA simulations is derived from the stiffness of the printed material k_{exp} through Eq. (9) and is equal to 1.063 GPa. In addition, the elements used to mesh the samples are triangular elements of first degree. Their size is defined in the following with a FEA meshing convergence study.

$$E_{FEA} = \frac{k_{exp} * height_{sample}}{width_{sample} * thickness_{sample}} \tag{9}$$

The nine samples are tested by FEA simulations using the FEA environment and using the following boundary conditions (Fig. 14).

- Uniaxial vertical displacement of intensity d_{FEA}, simulating compressive loading, applied on the top of the sample (Fig. 14a), that distorts the initial sample (Fig. 14b);
- Fixed connection on the bottom of the sample;
- Free everywhere else.

In the FEA simulations, a displacement d_{FEA} is imposed on the top of the samples and the resulting force F_{FEA} of the bottom of the samples is retrieved. Using these two quantities, the stiffness k^*_{FEA} (in N/mm) of the samples is computed (Eq. (10)). Thereafter, this stiffness is divided by the stiffness k_{FEA} equal to k_{exp} (Eq. (11) and section 4.3.1). Finally, for each of the nine samples studied through numerical simulations, the ratio r_{FEA} can be computed (Eq. (11)).

$$k^*_{FEA} = \frac{F_{FEA}}{d_{FEA}} \tag{10}$$

$$r_{FEA} = \frac{k^*_{FEA}}{k_{FEA}} \tag{11}$$

To verify that the FEA meshing conditions allow to describe accurately the resulting displacement of the sample, a FEA meshing convergence study is done (Fig. 15). For this convergence study, one of the patterns that provides the thinnest struts is considered: the RE-EL pattern of couple $(0.45; 30°)$. The convergence study shows that convergence in the resulting displacement appears with three meshing elements in the thinnest struts. Thus, in the following, four elements in the thinnest struts of the samples are used to ensure the

Table 2
Parameters of the nine printed samples and their mass analysis.

PSDMR	SQ-EL			RE-EL			RE-TR		
v_f	0.5	0.6	0.6	0.6	0.5	0.6	0.1	0.2	0.1
β	0	0	45	0	30	30	0	0	30
Sample number	#1	#2	#3	#4	#5	#6	#7	#8	#9
Theoretical volume (mm^3)	42,504	47,994	47,082	45,755	43,592	49,071	15,441	21,502	16,074
Theoretical mass (g)	55.10	62.22	61.04	59.32	56.51	63.61	20.02	27.87	20.77
Printed mass (g)	55.61	61.21	63.13	58.70	57.09	66.01	19.97	27.8	20.77
Delta mass (%)	0.93	1.62	3.43	1.03	1.03	3.77	0.25	0.25	0.33

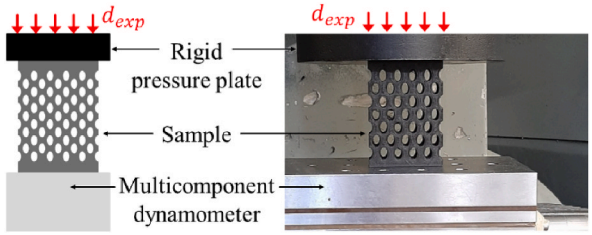

Fig. 13. Testing bench used to induce compression loadings to the samples.

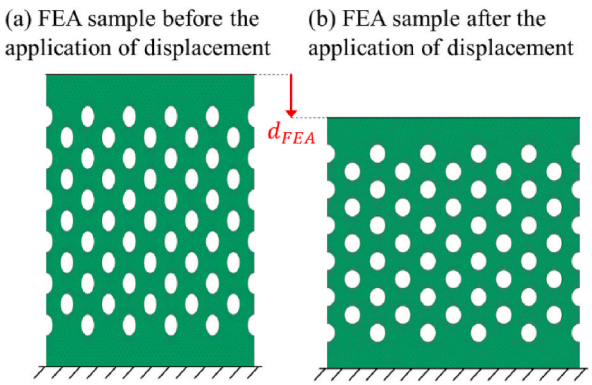

Fig. 14. Boundary conditions used in the FEA simulations applied on a material removed sample through a SQ-EL pattern of couple $(0.7;\ 0°)$: fixed connection at the bottom of the sample and imposed displacement d_{FEA} at the top of the sample.

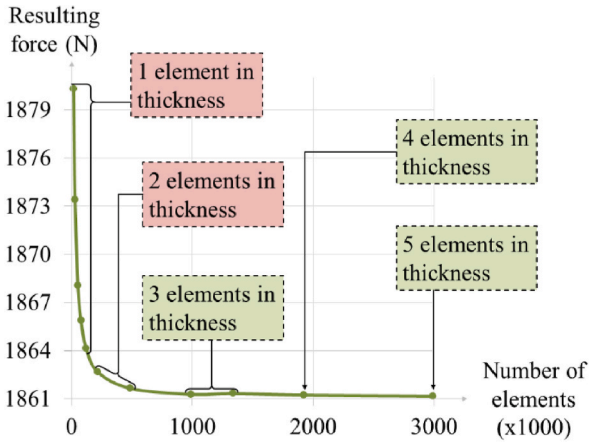

Fig. 15. Convergence study of the finite element meshing.

accuracy of the simulations to describe the resulting force F_{FEA}.

Once the relative stiffness of the nine samples r_{FEA} and r_{exp} are computed, they are compared. On Fig. 16 is plotted the relative longitudinal stiffnesses for all the nine samples obtained from experimental tests and FEA simulations presented previously. For each sample, the couple of parameters $(v_f;\ \beta)$ is also presented. First, it can be observed that the relative longitudinal stiffnesses follow the same trend. Second, to quantify this similarity, it is chosen to compare the standard deviation of the phenomenon in FEA simulations (0.185 N/mm) and the standard deviation between the FEA simulations and the experimental tests (0.017 N/mm). This difference shows that the relative stiffness is well represented by the FEA simulations. For this reason, the presented FEA environment and parameters are validated for the purpose of the study and used in section 4.4.

4.4. PSDMR pattern performance evaluation

This section focuses on the comparison of the mechanical performance of the three different PSDMR patterns (section 3.3) using

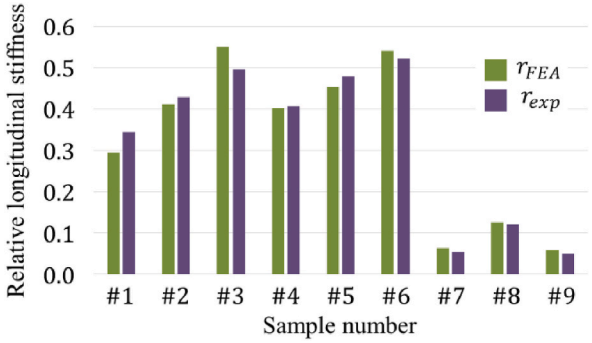

Fig. 16. Summarize of the relative stiffness of the different samples tested by FEA simulations r_{FEA} and by experiments r_{exp} for the three PSDMR pattern, for different volume fraction v_f and structural anisotropy orientation β.

different couples $(v_f;\ \beta)$ (green boxes in Table 1) under uniaxial compression. The purpose of this comparison is the definition of the most suitable domain of use for each pattern in porous structures in terms of mechanical stiffness.

These tests are conducted by Finite Element Analysis (FEA) simulations using the FEA environment presented and validated in section 4.3 and using homogeneous material FEA condition.

4.4.1. Longitudinal stiffness

In order to evaluate the mechanical performances of the three patterns, the study must focus on a unit cellular pattern. In addition, a mechanical performance indicator must be defined.

In the following, the performance evaluated is the mechanical stiffness of the patterns represented by their moduli of elasticity. Particularly, the patterns being anisotropic due to the induced structural anisotropy (section 2.3.2), the stiffness is represented hereafter by the longitudinal modulus of elasticity E^*. It corresponds to the Young's modulus of the pattern in the studied direction (here, along the vertical axis). Hereafter, this longitudinal modulus of elasticity E^* is calculated using the Hooke's law in linear elasticity (Eq. (12)) between the two extreme points P_1 and P_2. These two points have an initial coordinate z_i (Fig. 17a) and a deformation Δz_i along the vertical **z**-axis (Fig. 17b and Eq. (13)). The resulting modulus E^* (Eq. (14) where l is the width of the structure and e the thickness) is then divided by the Young's modulus of the material without hole E used in the FEA to obtain the relative longitudinal stiffness R (Eq. (15)) of the PSDMR pattern.

$$\sigma = \frac{F}{S} = \frac{F}{l * e} = E^* * \varepsilon = E^* * \frac{\Delta L}{L_0} \tag{12}$$

$$\frac{F}{l * e} = E^* * \frac{|\Delta z_2 - \Delta z_1|}{|z_2 - z_1|} \tag{13}$$

$$E^* = \frac{F * |z_2 - z_1|}{l * e * |\Delta z_2 - \Delta z_1|} \tag{14}$$

$$R = \frac{E^*}{E} \tag{15}$$

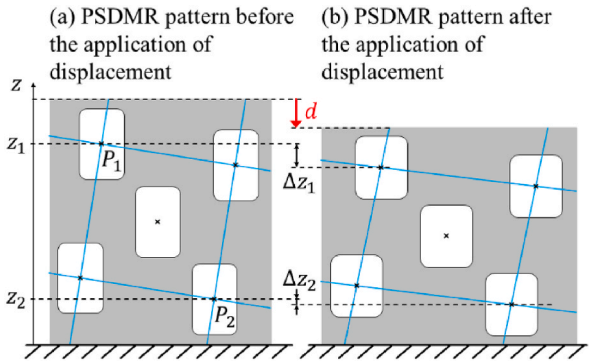

Fig. 17. Initial topology (a) and deformation (b) of a general PSDMR pattern respectively before and after compression loads are faced.

4.4.2. FEA set-up: designed structure and boundary conditions

To study the longitudinal modulus of elasticity E^* of a unit cellular pattern, two possibilities exist:

- Study of a unit cellular PSDMR pattern that has specific boundary conditions, called "representative volume element" (RVE) [25,57,58]. These boundary conditions represent the surrounding unit cellular patterns;
  -Study of a unit cellular PSDMR pattern surrounded by a sufficient number of unit cellular patterns. This way is used hereafter. Several studies highlighted that a repetition of $8 * 8$ unit cellular patterns are enough to represent the phenomenon [56,59]. Thus in this study, a repetition of $10 * 10$ unit cellular patterns is done (Fig. 18). This hypothesis is validated in the following (Fig. 19).

As explained in section 4.3, the FEA environment and its associated parameters are suitable for this performance investigation. Thus, the FEA simulations conducted on the patterns are the same as the one describe in section 4.3, except for the boundary conditions. Indeed, the studied designs differ, so the boundary conditions must be adapted (Fig. 18).

- Sliding contacts on the left side of the structure (only vertical translation is allowed, all rotations are blocked);
- Sliding contacts on the bottom part of the structure (only lateral translation is allowed, all rotations are blocked);
- Uniform compression force is applied on the top of the structure.

Fig. 19 highlights the stability of the results in the central part of the PSDMR pattern. Indeed, the two rows of unit cellular patterns surrounding the studied one present stable results, which entails the accuracy of the results of the studied unit cellular pattern. This validates that repeating the unit cellular patterns 10 times ensures the accuracy of the results.

4.4.3. Results

In this comparison study, every PSDMR patterns that present structural cohesion (Table 1) are tested through the FEA simulation process presented in section 4.4.2. For each pattern, the relative longitudinal stiffness R (section 4.4.1) is calculated as a function of three parameters:

- The PSDMR pattern itself;
- The volume fraction v_f;
- The structural anisotropy orientation β.

These results are presented in Table 3 to be compared in the following. These data are then plotted independently regarding the PSDMR patterns: SQ-EL pattern (Fig. 20a), RE-EL pattern (Fig. 20b) and the RE-TR pattern (Fig. 20c). It plots the relative longitudinal stiffness R of each pattern as a function of its volume fraction v_f (varying from 0.05 to 0.95) and its structural anisotropy orientation β (varying from 0° to 45° and from 0° to 30°). It allows to highlight the influence of β on the mechanical performance of the PSDMR pattern.

All the data of the three PSDMR patterns (presented in Table 3) are plotted on a same 2D graph (Fig. 20d). For a better visualisation of the data, they are also plotted on a 3D surface graph (Fig. 21a). A top view of this surface graph is plotted in Fig. 21b. This 3D graph is suitable to identify which PSDMR pattern has the greater relative longitudinal stiffness R for a given couple $(v_f;\ \beta)$. On the one hand, the square-shaped grid has an angular periodicity of 90° while on the other hand, the rectangular-shaped grid has an angular periodicity of 60° (section 3.1). As a consequence, their mutual periodicity is 180°. In fact, a symmetric exists between the angular ranges $[0°;\ 90°]$ and $[90°; 180°]$. For this reason, in Fig. 21, the comparison is done for angles varying in the range $[0°;\ 90°]$.

5. Discussion

The results showed in Table 3 highlights that the factor with the greatest influence on the mechanical performances of the PSDMR pattern is the volume fraction v_f. Indeed, a direct link between the relative longitudinal stiffness R and the volume fraction v_f exists. To validate this assumption, the results are best-fitted with a parabola R_{model} using the least square method (Eq. (16)). From this model, the conclusion that it allows to model 80% of the relative longitudinal stiffness can be drawn (as presented in Ref. [60]). Moreover, it is highlighted on Fig. 21 that the choices of the used pattern and the structural anisotropy orientation still have a significant influence on the relative longitudinal stiffness. Indeed, it has a different influence depending on the pattern studied. It is highlighted in Fig. 20a that the SQ-EL pattern tends to have a large variation of performance depending on its structural anisotropy orientation. On the contrary, the RE-TR pattern seems to be little influenced by the structural anisotropy orientation, it seems to be an isotropic pattern, comforting what could be found in the literature [61] (Fig. 20c).

$$R_{model} = k * {v_f}^2 \text{ with } k \text{ a constant} \tag{16}$$

In addition, the structural anisotropy orientation β coupled with the volume fraction v_f have an influence on the structural cohesion of the pattern and thus on its mechanical performances (section 4.2). Indeed, it can be observed in Table 3, Figs. 20a and b that the patterns have specific couple $(v_f;\ \beta)$ from which they present structural cohesion. It tends to show that the greater the structural anisotropy orientation, the greater the volume fraction threshold that ensure structural cohesion. These cohesion differences influence the mechanical performances of the patterns because unlike the SQ-EL or RE-EL patterns, the RE-TR pattern has structural cohesion for

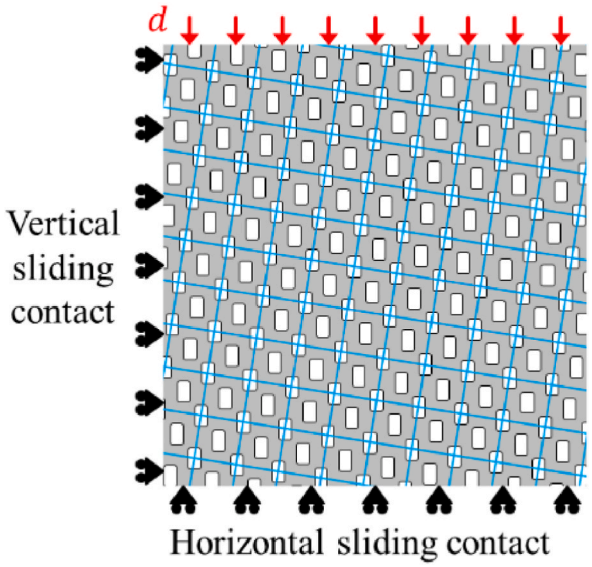

Fig. 18. Example of a structure made of a PSDMR pattern repeated 10 time in both planar directions.

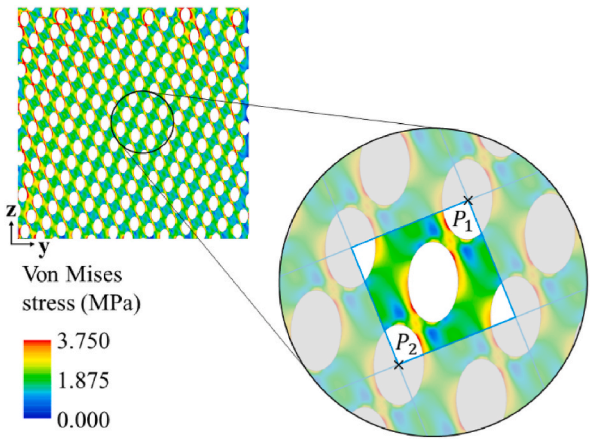

Fig. 19. Unit cellular pattern isolated from the central area of a structure made of SQ-EL pattern of parameters (0.6; 22.5°).

every couple $(v_f;\ \beta)$. Therefore, the performances of the RE-TR pattern are better compare to the one of the other two patterns in the range of v_f and β where the structural cohesion is lost or close to be lost. Thus, below a volume fraction equal to 0.42, it seems that the RE-TR pattern presents a better relative longitudinal stiffness R. However, it seems that this threshold is independent to the structural anisotropy orientation β. Above this threshold, the SQ-EL and RE-EL patterns seems to perform better than the RE-TR pattern. So, the patterns must be compared in the range $\{v_f \epsilon [0.42; 1];\ \beta \epsilon [0°; 90°]\}$.

In this region, Fig. 21 illustrates that the SQ-EL pattern has a performance peak on the range $\{v_f \epsilon [0.55; 0.95];\ \beta \epsilon [30°; 70°]\}$, in which the pattern has better average performances than RE-EL (5%) and RE-TR (21%).

From a global stand point, the study of the influence of the different parameters $\{v_f \epsilon [0; 1];\ \beta \epsilon [0°; 90°]\}$ on the relative longitudinal stiffness of the patterns of the PSDMR patterns lead to the following suitable domain of use:

- In domain n°1, the RE-TR pattern has better performances than the SQ-EL and RE-EL pattern due to their structural cohesion issues;
- On the range $\{v_f \epsilon [0.55; 0.95];\ \beta \epsilon [30°; 70°]\}$, the SQ-EL pattern present a performance peak and has better performances than the other patterns;
- In domain n°2, the RE-EL pattern has better performances than the two other patterns;
- In domain n°1, the RE-TR pattern has better performances than the two other patterns.

To compare the two bone bio-inspired patterns (SQ-EL and RE-EL), on the one hand RE-EL presents better longitudinal stiffness for structural anisotropy orientation β around 0° and 90°; which corresponds to stress orientations nearly aligned to the two grid vectors **u**

Table 3
Presentation of the different relative longitudinal stiffness R for every PSDMR pattern with the different studied couples $(v_f;\ \beta)$

v_f	SQ-EL Square grid + Ellipse holes $\beta_{SQ\text{-}EL}$					RE-EL Rectangular grid + Ellipse holes $\beta_{RE\text{-}EL}$					RE-TR Rectangular grid + Triangular holes $\beta_{RE\text{-}TR}$				
	0°	11.25°	22.5°	33.75°	45°	0°	7.5°	15°	22.5°	30°	0°	7.5°	15°	22.5°	30°
0.05	/	/	/	/	/	/	/	/	/	/	0.017	0.015	0.015	0.015	0.019
0.10	/	/	/	/	/	/	/	/	/	/	0.034	0.029	0.028	0.034	0.036
0.15	0.004	/	/	/	/	/	/	/	/	/	0.053	0.046	0.049	0.051	0.055
0.20	0.017	/	/	/	/	/	/	/	/	/	0.072	0.064	0.069	0.070	0.076
0.25	0.038	/	/	/	/	0.012	/	/	/	/	0.093	0.084	0.089	0.090	0.097
0.30	0.064	0.017	/	/	/	0.035	/	/	/	/	0.115	0.111	0.111	*0.111*	*0.120*
0.35	0.097	0.044	/	/	/	0.070	0.074	/	/	/	0.140	0.134	0.133	*0.134*	0.144
0.40	0.131	0.088	0.008	/	/	0.112	0.128	0.144	/	/	0.164	0.162	0.161	0.160	0.170
0.45	0.174	0.156	0.107	/	/	0.165	0.190	0.240	0.302	0.373	0.195	0.188	0.188	0.190	0.199
0.50	0.218	0.213	0.210	0.216	/	0.220	0.251	0.297	0.341	0.387	0.227	0.219	0.220	0.223	0.229
0.55	0.272	0.270	0.300	0.400	0.469	0.281	0.314	0.367	0.393	0.430	0.263	0.254	0.256	0.258	0.267
0.60	0.320	0.335	0.376	0.471	0.505	0.350	0.365	0.406	0.444	0.466	0.342	0.293	0.295	0.300	0.306
0.65	0.389	0.397	0.453	0.529	0.547	0.426	0.440	0.471	0.495	0.519	0.346	0.340	0.341	0.343	0.350
0.70	0.460	0.479	0.526	0.589	0.593	0.495	0.508	0.531	0.552	0.571	0.403	0.397	0.396	0.399	0.405
0.75	0.533	0.550	0.586	0.636	0.637	0.567	0.571	0.588	0.559	0.611	0.451	0.452	0.460	0.458	0.458
0.80	0.619	0.641	0.659	0.702	0.695	0.649	0.648	0.662	0.671	0.682	0.533	0.537	0.530	0.525	0.532
0.85	0.704	0.720	0.734	0.763	0.761	0.724	0.723	0.731	0.734	0.736	0.602	0.616	0.615	0.615	0.614
0.90	0.799	0.807	0.820	0.831	0.828	0.812	0.809	0.812	0.812	0.819	0.740	0.738	0.739	0.724	0.719
0.95	0.898	0.899	0.904	0.907	0.907	0.901	0.895	0.901	0.899	0.902	0.848	0.853	0.872	0.855	0.855

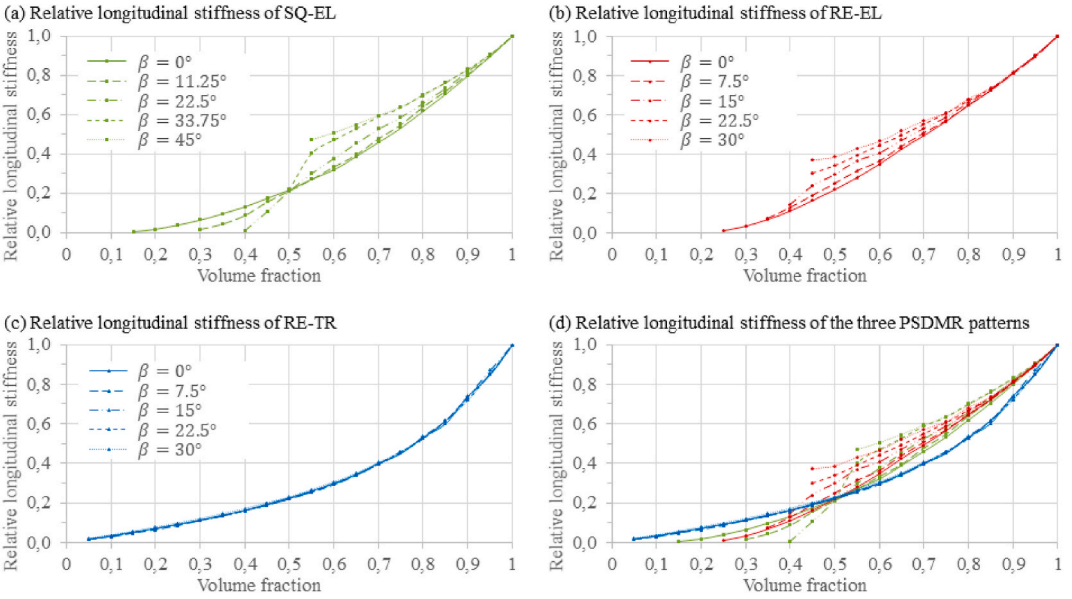

Fig. 20. Relative longitudinal stiffness for each pattern tested: SQ-EL pattern (a), RE-EL pattern (b), RE-TR pattern (c); and the all three combined (d).

and **v.** On the other hand, for structural anisotropy orientation β around 45°, SQ-EL has better relative longitudinal stiffness.

In addition to these points, the presented study has three main limitations.

- First, the number of tested pattern may be criticized. However, the three patterns have been selected for their presumed mechanical performances. The first pattern being bio-inspired from bone and taken from literature, the interest of such a pattern had been already exposed. The second pattern, that has been developed in this paper, is also bio-inspired from bone and was presented as an improvement of the first one. Indeed, this study showed that this second bio-inspired pattern has indeed better mechanical performances for specific couple of parameters $(v_f;\ \beta)$. The third pattern is also taken from the literature and has been selected for its isotropic properties;
- Second, the accuracy of the performance domains may also be improved. Indeed, following the current repartition of the performance domains, some couple of parameters may suggest the use of a pattern that is not the best from a performance point of view (for example with the couple $(0.45, 60°)$). However, for these particular couple of parameters, the relative longitudinal stiffness is really close (peak of difference equal to 15%). So the error made on the accuracy of the domains is quite small;

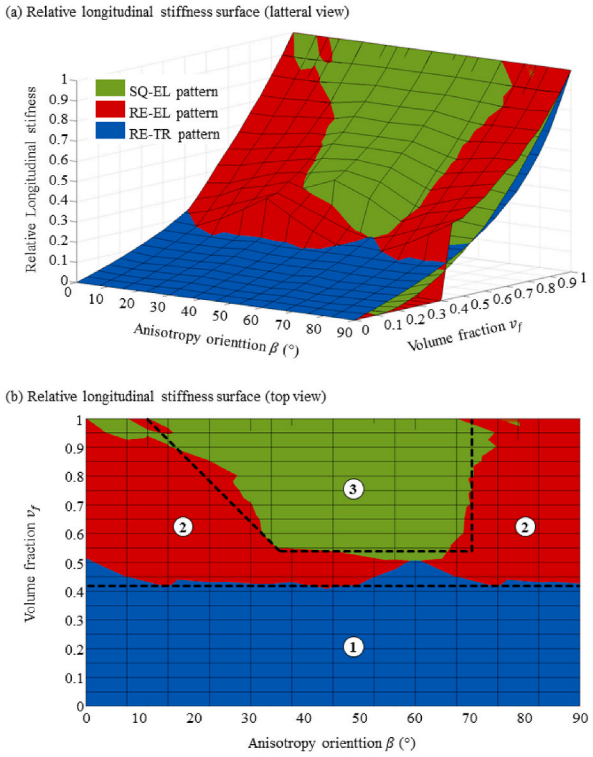

Fig. 21. Relative longitudinal stiffness of the three PSDMR pattern plotted on a 3D surface graph from the side view (a) and the top view (b). On the top view, the performance domains of PSDMR patterns are highlighted (black dotted lines and numbered).

- Third, extended studies may be carried out including the submission of the PSDMR patterns to other mechanical loadings.

6. Conclusion

This paper proposed to establish the performance domains of three planar Periodic Stress-Driven Material Removal (PSDMR) patterns. These patterns, which are considered as cellular structures, may be used in stress-driven material removing methods. The first one is bio-inspired from long bone trabecular structure which have shown good mechanical stiffness performances vs material removal (SQ-EL pattern). It is made of a square shaped grid and elliptic holes, both bio-inspired from long bones. The second one, is also bone bio-inspired and is *a priori* an improvement of the first one in terms of mechanical stiffness performances vs material removal (RE-EL pattern). This one is based on rectangular shaped grid (which represents a hexagonal grid) and elliptical holes. The third one is a strut-based lattice pattern (RE-TR pattern). This third pattern is made of a rectangular-shaped grid and triangular holes. It is studied for its isotropic behavior. These three patterns have been tested under compressive loading through finite element analysis (FEA) simulations. The mechanical performances is quantified in this study by the relative longitudinal stiffness. In the same time, the parameters of the FEA simulations are validated by testing nine samples on an experimental compressive bench test. This study showed that the mechanical performances of the three patterns are influenced by two parameters from stress-driven material removing methods: the volume fraction of the pattern v_f and the structural anisotropy orientation of the pattern β. The following main conclusions may be drawn from this paper:

- The volume fraction of the pattern is the factor that has the greatest influence on the mechanical performance;
- The choice of the grid topology, the volume fraction and the structural anisotropy orientation of pattern have a great influence on its structural cohesion;
- The two bone bio-inspired patterns (SQ-EL and RE-EL) present a cohesion loss for specific couple of parameter $(v_f; \beta)$. However, this cohesion is ensured for any couple $(v_f; \beta)$ with the strut-based lattice pattern (RE-TR);
- For low volume fractions (below 0.42), the strut-based lattice pattern (RE-TR) presents the best mechanical performance independently to the structural anisotropy orientation;
- For volume fractions above 0.42, two bone bio-inspired patterns (SQ-EL and RE-EL) present the best overall mechanical performance depending on the structural anisotropy orientation: the RE-EL pattern performs better in the domain n°2 and the SQ-EL pattern performs better in the domain n°3;
- To compare the two bone bio-inspired patterns, on the one hand the pattern based on a rectangular grid (RE-EL) presents better longitudinal stiffness for structural anisotropy orientation β around 0° and 90°; which corresponds to stress orientations nearly

aligned to the two grid vectors. On the other hand, for structural anisotropy orientation β around 45°, square grid based pattern (SQ-EL) has better mechanical performances.

Finally, in a context of stress-driven material removing material method, using this study and depending on the local parameters, it is possible to select the pattern that has the best longitudinal stiffness to reduce the mass of a part while managing the decrease of its mechanical performances.

This study opens up outlooks for possible developments of designing mass reduced structures based on adaptive stress-driven material removal pattern to combine the performance of the three tested patterns. In addition, the mechanical performances of the bio-inspired patterns highlighted in this study are engaging for extending these patterns to 3- dimensions.

Data availability statement

Data will be made available on request.

CRediT authorship contribution statement

Mathieu Bilhère-Dieuzeide: Writing – original draft, Writing – review & editing, Software, Resources, Methodology, Investigation, Formal analysis, Data curation, Conceptualization. **Julien Chaves-Jacob:** Writing – original draft, Writing – review & editing, Visualization, Validation, Supervision, Software, Resources, Project administration, Methodology, Investigation, Funding acquisition, Formal analysis, Data curation, Conceptualization. **Emmanuel Buhon:** Writing – review & editing, Validation, Supervision, Software, Resources, Project administration, Methodology, Investigation, Funding acquisition, Formal analysis, Conceptualization. **Guillaume Biguet-Mermet:** Writing – review & editing, Validation, Supervision, Software, Resources, Project administration, Methodology, Investigation, Funding acquisition, Formal analysis, Conceptualization. **Jean-Marc Linares:** Writing – original draft, Writing – review & editing, Visualization, Validation, Supervision, Project administration, Methodology, Investigation, Funding acquisition, Formal analysis, Conceptualization.

Declaration of Competing interest

The authors declare that they have no known competing financial interests or personal relationships that could have appeared to influence the work reported in this paper.

Acknowledgment

The experimental equipment was funded by the European Community, French Ministry of Research and Education and Aix-Marseille Conurbation Community. Authors acknowledge the Association Nationale Recherche Technologie (France) for financial support through a Convention Industrielle de Formation par la Recherche fund (Cifre thesis n°2020/0881). Authors would like to thank Martin Egiziano who carried the experimental trials presented in section 4.3.1 of the paper.

References

[1] J.D. Deaton, R.V. Grandhi, A survey of structural and multidisciplinary continuum topology optimization: post 2000, Struct. Multidiscip. Optim. 49 (2014) 1–38, https://doi.org/10.1007/s00158-013-0956-z.
[2] Q. Xia, T. Shi, S. Liu, M.Y. Wang, A level set solution to the stress-based structural shape and topology optimization, Comput. Struct. 90–91 (2012) 55–64, https://doi.org/10.1016/j.compstruc.2011.10.009.
[3] P.D. Dunning, C.J. Brampton, H.A. Kim, Simultaneous optimization of structural topology and material grading using level set method, Mater. Sci. Technol. 31 (8) (2015) 884–894, https://doi.org/10.1179/1743284715Y.0000000022.
[4] E. Tyflopoulos, M. Steinert, Topology and parametric optimization-based design processes for lightweight structures, Appl. Sci. 10 (13: 4496) (2020), https://doi.org/10.3390/app10134496.
[5] H. Li, T. Yamada, P. Jolivet, K. Furuta, T. Kondoha, K. Izui, S. Nishiwaki, Full-scale 3D structural topology optimization using adaptive mesh refinement based on the level-set method, Finite Elem. Anal. Des. 194 (103561) (2021), https://doi.org/10.1016/j.finel.2021.103561.
[6] W.P. Syam, W. Jianwei, B. Zhao, I. Maskery, W. Elmadih, R. Leach, Design and analysis of strut-based lattice structures for vibration isolation, Precis. Eng. 52 (2018) 494–506, https://doi.org/10.1016/j.precisioneng.2017.09.010.
[7] T. Yu, H. Hyer, Y. Sohn, Y. Bai, D. Wu, Structure-property relationship in high strength and lightweight AlSi10Mg microlattices fabricated by selective laser melting, Mater. Des. 182 (2019) 108062, https://doi.org/10.1016/j.matdes.2019.108062.
[8] G. Dong, Y. Tang, Y.F. Zhao, A survey of modeling of lattice structures fabricated by additive manufacturing, J. Mech. Des. 139 (10) (2017) 100906, https://doi.org/10.1115/1.4037305.
[9] Z. Xiao, Y. Yang, R. Xiao, Y. Bai, C. Song, D. Wang, Evaluation of topology-optimized lattice structures manufactured via selective laser melting, Mater. Des. 143 (2018) 27–37, https://doi.org/10.1016/j.matdes.2018.01.023.
[10] A. Nazir, K.M. Abate, A. Kumar, J.Y. Jeng, A state-of-the-art review on types, design, optimization, and additive manufacturing of cellular structures, Int. J. Adv. Des. Manuf. Technol. 104 (2019) 3489–3510, https://doi.org/10.1007/s00170-019-04085-3.
[11] S. Duan, L. Xi, W. Wen, D. Fang, Mechanical performance of topology-optimized 3D lattice materials manufactured via selective laser sintering, Compos. Struct. 238 (2020) 111985, https://doi.org/10.1016/j.compstruct.2020.111985.
[12] A. Kumar, L. Collini, A. Daurel, J.-Y. Jeng, Design and additive manufacturing of closed cells from supportless lattice structure, Addit. Manuf. 33 (101168) (2020), https://doi.org/10.1016/j.addma.2020.101168.
[13] H. Yin, Z. Liu, J. Dai, G. Wen, C. Zhang, Crushing behavior and optimization of sheet-based 3D periodic cellular structures, Composites, Part B 182 (2020) 107565, https://doi.org/10.1016/j.compositesb.2019.107565.

[14] G.J. Shah, A. Nazir, S.-C. Lin, J.-Y. Jeng, Design for additive manufacturing and investigation of surface-based lattice structures for buckling properties using experimental and finite element methods, Materials 15 (4037) (2022), https://doi.org/10.3390/ma15114037.
[15] O. Al-Ketan, R. Rowshan, R.K.A. Al-Rub, Topology-mechanical Property Relationship of 3D Printed Strut, Skeletal, and Sheet Based Periodic Metallic Cellular Materials, Additive Manufacturing 19, 2018, pp. 167–183, https://doi.org/10.1016/j.addma.2017.12.006.
[16] A. Nazir, J.-Y. Jeng, Buckling behavior of additively manufactured cellular columns: experimental and simulation validation, Mater. Des. 186 (2020) 108349, https://doi.org/10.1016/j.matdes.2019.108349.
[17] S.P. Soe, P. Martin, M. Jones, M. Robinson, P. Theobald, Feasibility of optimising bicycle helmet design safety through the use of additive manufactured TPE cellular structures, Int. J. Adv. Des. Manuf. Technol. 79 (2015) 1975–1982, https://doi.org/10.1007/s00170-015-6972-y.
[18] D.W. Abueidda, M. Elhebeary, C.-S.A. Shiang, S. Pang, R.K.A. Al-Rub, I.M. Jasiuk, Mechanical properties of 3D printed polymeric gyroid cellular structures: experimental and finite element study, Mater. Des. 165 (2019) 107597, https://doi.org/10.1016/j.matdes.2019.107597.
[19] D. Sharma, S.S. Hiremath, Bio-inspired repeatable lattice structures for energy absorption: experimental and finite element study, Compos. Struct. 283 (115102) (2022), https://doi.org/10.1016/j.compstruct.2021.115102.
[20] T. Yu, X. Li, M. Zhao, X. Guo, J. Ding, S. Qu, T.W.J. Kwok, T. Li, X. Song, B.W. Chua, Topology-mechanical property relationship of 3D printed strut, skeletal, and sheet based periodic metallic cellular materials, Mater. Today Commun. 35 (106344) (2023), https://doi.org/10.1016/j.mtcomm.2023.106344.
[21] W. Tang, C. Zou, H. Zhou, L. Zhang, Y. Zeng, L. Sun, Y. Zhao, M. Yan, J. Fu, J. Hu, Z. Li, Z. Liu, T. Wang, Z. Zhang, A novel convective heat transfer enhancement method based on precise control of Gyroid-type TPMS lattice structure, Appl. Therm. Eng. 230 (2023) 120797, https://doi.org/10.1016/j.applthermaleng.2023.120797.
[22] K. Yeranee, Y. Rao, A review of recent investigations on flow and heat transfer enhancement in cooling channels embedded with Triply Periodic Minimal Surfaces (TPMS), Energies 15 (8994) (2022), https://doi.org/10.3390/en15238994.
[23] D. Li, N. Dai, Y. Tang, G. Dong, Y.F. Zhao, Design and optimization of graded cellular structures with triply periodic level surface-based topological shapes, J. Mech. Des. 141 (71402) (2019), https://doi.org/10.1115/1.4042617.
[24] S. Catchpole-Smith, R.R.J. Sélo, A.W. Davis, I.A. Ashcroft, C.J. Tuck, A. Clare, Thermal conductivity of TPMS lattice structures manufactured via laser powder bed fusion, Addit. Manuf. 30 (2019) 100846, https://doi.org/10.1016/j.addma.2019.100846.
[25] D. Da, J. Yvonnet, L. Xia, M.V. Le, G. Li, Topology optimization of periodic lattice structures taking into account strain gradient, Comput. Struct. 210 (2018) 28–40, https://doi.org/10.1016/j.compstruc.2018.09.003.
[26] Y.M. Xie, Z.H. Zuo, X. Huang, J.H. Rong, Convergence of topological patterns of optimal periodic structures under multiple scales, Struct. Multidiscip. Optim. 46 (2012) 41–50, https://doi.org/10.1007/s00158-011-0750-8.
[27] Z.H. Zuo, X. Huang, X. Yang, J.H. Rong, Y.M. Xie, Comparing optimal material microstructures with optimal periodic structures, Comput. Mater. Sci. 69 (2013) 137–147, https://doi.org/10.1016/j.commatsci.2012.12.006.
[28] A. Panesar, M. Abdi, D. Hickman, I. Ashcroft, Strategies for Functionally Graded Lattice Structures Derived Using Topology Optimisation for Additive Manufacturing, Additive Manufacturing, vol. 19, 2018, pp. 81–94, https://doi.org/10.1016/j.addma.2017.11.008.
[29] Y. Wang, L. Zhang, S. Daynes, H. Zhang, S. Feih, M.Y. Wang, Design of graded lattice structure with optimized mesostructures for additive manufacturing, Mater. Des. 142 (2018) 114–123, https://doi.org/10.1016/j.matdes.2018.01.011.
[30] J. Robbins, S.J. Owen, B.W. Clark, T.E. Voth, An Efficient and Scalable Approach for Generating Topologically Optimized Cellular Structures for Additive Manufacturing, Additive Manufacturing, vol. 12, 2016, pp. 296–304, https://doi.org/10.1016/j.addma.2016.06.013.
[31] F. Liu, M. Chen, L. Wang, T. Luo, G. Chen, Stress-field driven conformal lattice design using circle packing algorithm, Heliyon 9 (e14448) (2023), https://doi.org/10.1016/j.heliyon.2023.e14448.
[32] D. Kang, S. Park, Y. Son, S. Yeon, S.H. Kim, I. Kim, Multi-lattice inner structures for high-strength and light-weight in metal selective laser melting process, Mater. Des. 175 (2019) 107786, https://doi.org/10.1016/j.matdes.2019.107786.
[33] Y.M. Hailu, A. Nazir, S.-C. Lin, J.-Y. Jeng, The effect of functional gradient material distribution and patterning on torsional properties of lattice structures manufactured using multijet fusion technology, Materials 14 (6521) (2021), https://doi.org/10.3390/ma14216521.
[34] M. Xiao, X. Liu, Y. Zhang, L. Gao, J. Gao, S. Chu, Design of graded lattice sandwich structures by multiscale topology optimization, Comput. Methods Appl. Mech. Eng. 384 (2021) 113949, https://doi.org/10.1016/j.cma.2021.113949.
[35] D. Li, W. Liao, N. Dai, Y.M. Xie, Anisotropic design and optimization of conformal gradient lattice structures, Comput. Aided Des. 119 (2020) 102787, https://doi.org/10.1016/j.cad.2019.102787.
[36] M. Zou, S. Xu, C. Wei, H. Wang, Z. Liu, A bionic method for the crashworthiness design of thin-walled structures inspired by bamboo, Thin-Walled Struct. 101 (2016) 222–230, https://doi.org/10.1016/j.tws.2015.12.023.
[37] L. Tadrist, Y. Mammadi, J. Diperi, J.-M. Linares, Deformation and mechanics of a pulvinus-inspired material, Bioinspiration Biomimetics 17 (65002) (2022), https://doi.org/10.1088/1748-3190/ac884f.
[38] S.F. Fischer, M. Thielen, R.R. Loprang, R. Seidel, C. Fleck, T. Speck, A. Bührig-Polaczek, Pummelos as concept generators for biomimetically inspired low weight structures with excellent damping properties, Adv. Eng. Mater. 12 (12) (2010) 658–663, https://doi.org/10.1002/adem.201080065.
[39] M.C. Fernandes, J. Aizenberg, J.C. Weaver, K. Bertoldi, Mechanically robust lattices inspired by deep-sea glass sponges, Nat. Mater. 20 (2021) 237–241, https://doi.org/10.1038/s41563-020-0798-1.
[40] G. Chouhan, B.M. Gunji, P. Bidare, D. Ramakrishna, R. Kumar, Experimental and numerical investigation of 3D printed bio-inspired lattice structures for mechanical behaviour under quasi static loading conditions, Mater. Today Commun. 35 (2023) 105658, https://doi.org/10.1016/j.mtcomm.2023.105658.
[41] Y. Seki, M.S. Schneider, M.A. Meyers, Structure and mechanical behavior of a toucan beak, Acta Mater. 53 (2005) 5281–5296, https://doi.org/10.1016/j.actamat.2005.04.048.
[42] Z. Wang, N. Wu, Q. Wang, Y. Li, Q. Yang, F. Wu, Novel bionic design method for skeleton structures based on load path analysis, Appl. Sci. 10 (22: 8251) (2020), https://doi.org/10.3390/app10228251.
[43] J.C. Najmon, D.J. Jacob, Z.M. Wood, A. Tovar, Cellular helmet liner design through bio-inspired structures and topology optimization of compliant mechanism lattices, SAE International Journal of Transportation Safety 6 (3) (2018) 217–236. WCX18 Best Papers Special Issue, https://www.jstor.org/stable/26789716.
[44] G. Chouhan, B.M. Gunji, P. Bidare, D. Ramakrishna, R. Kumar, Experimental and numerical investigation of 3D printed bio-inspired lattice structures for mechanical behaviour under quasi static loading conditions, Mater. Today Commun. 35 (2023) 105658, https://doi.org/10.1016/j.mtcomm.2023.105658.
[45] D. Sysaykeo, J.-M. Linares, E. Mermoz, Wear behavior of a bio-inspired bearing for off-center loads, JBE 17 (2020) 1251–1262, https://doi.org/10.1007/s42235-020-0107-3.
[46] S. Arroyave-Tobon, K. Marquez-Florez, P. Heymann, J.-M. Linares, Generative design of joint contact surfaces inspired by biological morphogenesis, CIRP Ann. - Manuf. Technol. 71 (2022) 125–128, https://doi.org/10.1016/j.cirp.2022.04.006.
[47] C. Audibert, J. Chaves-Jacob, J.-M. Linares, Q.-A. Lopez, Bio-inspired method based on bone architecture to optimize the structure of mechanical workspieces, Mater. Des. 160 (2018) 708–717, https://doi.org/10.1016/j.matdes.2018.10.013.
[48] A. Ghazlan, T. Nguyen, T. Ngo, S. Linforth, V.T. Le, Performance of a 3D printed cellular structure inspired by bone, Thin-Walled Struct. 151 (2020) 106713, https://doi.org/10.1016/j.tws.2020.106713.
[49] M. Bilhère-Dieuzeide, J. Chaves-Jacob, E. Buhon, G. Biguet-Mermet, J.-M. Linares, Stress-driven method bio-inspired by long bone structure for mechanical part mass reduction by removing geometry at macro and cell-unit scales, Mater. Des. 213 (110318) (2022), https://doi.org/10.1016/j.matdes.2021.110318.
[50] N. Cadoret, J. Chaves-Jacob, J.-M. Linares, Structural additive manufacturing parts bio-inspired from trabecular bone form-function relationship, Mater. Des. 231 (2023) 112029, https://doi.org/10.1016/j.matdes.2023.112029.
[51] P. Fratzl, R. Weinkamer, Nature's hierarchical materials, Prog. Mater. Sci. 52 (8) (2007) 1263–1334, https://doi.org/10.1016/j.pmatsci.2007.06.001.
[52] M. Bilhère-Dieuzeide, J. Chaves-Jacob, E. Buhon, G. Biguet-Mermet, J.-M. Linares, Material removal of hip stem prosthesis using bio-inspiration from trabecular bone, Procedia CIRP 110 (2022) 265–270, https://doi.org/10.1016/j.procir.2022.06.048.

[53] M.A. Meyers, P.-Y. Chen, A.Y.-M. Lin, Y. Seki, Biological materials: structure and mechanical properties, Prog. Mater. Sci. 53 (1) (2008) 1–206, https://doi.org/10.1016/j.pmatsci.2007.05.002.
[54] B. Lui, H. Cheng, M. Liu, W. Cao, K. Jiang, Adaptive anisotropic porous structure design and modeling for 2.5D mechanical parts, Mater. Des. 206 (2021) 109786, https://doi.org/10.1016/j.matdes.2021.109786.
[55] L. Zorzetto, D. Ruffoni, Wood-inspired 3D-printed helical composites with tunable and enhanced mechanical performance, Adv. Funct. Mater. 29 (1: 1805888), https://doi.org/10.1002/adfm.201805888..
[56] H. Xia, J. Meng, J. Liu, X. Ao, S. Lin, Y. Yang, Evaluation of the equivalent mechanical properties of lattice structures based on the finite element method, Materials 15 (2993) (2022), https://doi.org/10.3390/ma15092993.
[57] S.L. Omairey, P.D. Dunning, S. Sriramula, Development of an ABAQUS plugin tool for periodic RVE homogenization, Eng. Comput. 35 (2019) 567–577, https://doi.org/10.1007/s00366-018-0616-4.
[58] A. Fadeel, H. Abdulhadi, R. Srinivasan, A. Mian, ABAQUS plug-in finite element tool for designing and analyzing lattice cell structures, Adv. Eng. Software 169 (103139) (2022), https://doi.org/10.1016/j.advengsoft.2022.103139.
[59] S.R. de Galarreta, J.R.T. Jeffers, S. Ghouse, A validated finite element analysis procedure for porous structures, Mater. Des. 189 (2020) 108546, https://doi.org/10.1016/j.matdes.2020.108546.
[60] S.N. Musy, G. Maquer, J. Panyasantisuk, J. Wandel, P.K. Zysset, Not only stiffness, but also yield strength of the trabecular structure determined by non-linear μFE is best predicted by bone volume fraction and fabric tensor, J. Mech. Behav. Biomed. Mater. 65 (2017) 808–813, https://doi.org/10.1016/j.jmbbm.2016.10.004.
[61] A.-J. Wang, D.L. McDowell, In-plane stiffness and yield strength of periodic metal honeycombs, J. Eng. Mater. Technol. 126 (2004) 137–156, https://doi.org/10.1115/1.1646165.